

# Electronic structure and exchange interactions in altermagnetic $\text{MnGeP}_2$ in the quasiparticle-self-consistent $GW$ approach.

Ilteris K. Turan\* and Walter R L. Lambrecht†

*Department of Physics, Case Western Reserve University,  
10900 Euclid Avenue, Cleveland, OH 44106-7079, USA*

Jerome Jackson‡

*Scientific Computing Department, STCF Daresbury Laboratory, Warrington WA4 4AD, United Kingdom*

The quasiparticle self-consistent (QS)  $GW$  method is used to study the electronic band structure, optical dielectric function, and exchange interactions in chalcopyrite,  $I\bar{4}2d$ , structure  $\text{MnGeP}_2$ . The material is found to be an antiferromagnetic semiconductor with lowest direct gap of 2.44 eV at the  $\Gamma$  point and a lower indirect gap of 2.16 eV from  $\Gamma$  to  $M$ . The material is an altermagnet because the two magnetic atoms of opposite spin are related by a two-fold rotation operation perpendicular to the main 4-fold rotation inversion axis. The spin splittings along a low symmetry line like  $PN$  is sizable while at  $\mathbf{k}$ -points on the diagonal mirror planes or on the twofold symmetry axes the spin splitting is zero. The exchange interactions are calculated using a linear response approach. The antiferromagnetic exchange-interaction between nearest neighbors in the primitive unit cell is dominating and found to be slightly decreasing upon carrier doping but not sufficiently to change the interaction to become ferromagnetic. The bare (non-interacting) and interacting transverse spin susceptibilities, which provide interatomic site exchange interactions after averaging over the muffin-tin spheres, are calculated from the  $GW$  band structure and wave functions. From these exchange interactions, the spin wave spectra are obtained along the high symmetry lines and the Néel temperature is calculated using the mean-field, and Tyablikov estimations. The dielectric function and the optical absorption spectra are calculated including excitonic effects using the Bethe Salpeter equation. The exchange interactions around  $\text{Mn}_{\text{Ge}}$  defect sites is also studied. While we find it can generate ferromagnetic interactions with neighboring spins, we did not find direct evidence of producing an overall ferromagnetic phase. First, if Mn antisites are introduced by exchanging Mn with a nearby Ge, the interactions stay largely antiferromagnetic. Second, when we add additional Mn, in other words in Mn-rich stoichiometry, the  $\text{Mn}_{\text{Ge}}$  antisites produce a strong ferromagnetic interaction primarily with the Mn in the same basal plane but weaker ferromagnetic interaction with adjacent plane Mn. The interactions between regular lattice Mn stay antiferromagnetic as before and thus favor keeping the antiferromagnetic order along the  $[001]$  direction. Adding Mn antisites however does lead to a metallic band structure.

## I. INTRODUCTION

Room-temperature magnetic semiconductors would greatly enhance the field of spintronics by the possibility of controlling both the magnetic moment and the carrier concentration but have remained elusive so far. One possible route proposed in the past is to dope chalcopyrite semiconductors like  $\text{ZnGeP}_2$  or  $\text{CdZnP}_2$  with a magnetic transition metal element like Mn. Compared to doping Mn in GaAs or other III-V compounds, this has the advantage that Mn is a divalent element and can therefore be more readily introduced in a II-IV- $\text{V}_2$  compound. Doping of  $\text{CdGeP}_2$  and  $\text{ZnGeP}_2$  were reported to show ferromagnetic behavior [1–9] but density functional calculations predicted antiferromagnetic

order instead [10, 11]. Pure  $\text{MnGeP}_2$  and  $\text{MnGeAs}_2$  were also synthesized and grown by various epitaxial growth methods[12, 13] and found to exhibit ferromagnetic hysteresis. Recently, ferromagnetic resonance was observed in  $\text{MnGeP}_2$  bulk single crystals grown by a gradient freeze method [14]. However, the origin of the ferromagnetism in these systems is not clear. Density functional calculations found these systems to be antiferromagnets and Mahadevan and Zunger [11] explained that Mn in II-VI (and similarly in II-IV- $\text{V}_2$ ) compounds are expected to prefer antiferromagnetism because in the ferromagnetic state, there are no empty Mn d-orbitals on a neighboring Mn to hop onto from a given Mn atom. Based on their defect studies, they proposed that  $\text{Mn}_{\text{Ge}}$  anti-site defects could be responsible for the ferromagnetism. More generally, one might wonder whether carrier-mediated exchange interactions could tilt the balance in favor of ferromagnetism.

All previous computational studies of these materials were carried out within the framework of density

\* ilteris.turan@case.edu

† walter.lambrecht@case.edu

‡ jerome.jackson@stfc.ac.uk

functional theory (DFT), which typically underestimates band gaps and may underestimate magnetic moments. Here we present a study based on the quasiparticle-self-consistent  $GW$  (QSGW) method,[15, 16] which is based on the many-body perturbation theoretical (MBPT) approach of Hedin[17, 18] which evaluates the dynamical self-energy  $\Sigma = iGW$  in terms of the one-electron Green's function  $G$  and the screened Coulomb interaction  $W$ . Besides accurately predicting the band gaps, this method can also be extended to a linear response approach to extract the exchange interactions from the transverse spin susceptibility  $\chi^{+-}$  [19]. This method is used here to predict the Heisenberg-type exchange interactions without making *a-priori* assumptions on the type of ordering. Starting from a DFT+ $U$  calculation, we first stabilize a ferromagnetic state within QSGW without additional Hubbard- $U$ . The self-energy  $\Sigma$  of the QSGW method takes over the role of  $U$  and leads to occupied majority spin bands of Mn- $d$  being well separated from the minority spin states. The corresponding band structure shows an indirect band gap. The exchange interactions, however, indicate a strong antiferromagnetic coupling between the two Mn atoms in the primitive unit cell. This is the dominant exchange interaction found. Other longer range interactions between cells are much smaller. Based on this prediction, we then calculate the antiferromagnetic state within the same unit cell. The exchange interactions still predict antiferromagnetic coupling but are now more reliably calculated. We calculate the Néel temperature in the mean field approximation and using the Tyablikov method.[20–22]

To study the possibility of carrier-mediated ferromagnetism we essentially use a rigid band approach in which hole doping is introduced by changing the valence band filling compensated by a neutralizing homogeneous background. Similarly, we can also add n-type doping in the conduction band. Either of these methods are found to reduce the nearest neighbor antiferromagnetic exchange interaction but the effect is too small to flip the balance toward net ferromagnetism even for an unrealistically high doping concentration. On the other hand, the exchange interactions between  $\text{Mn}_{\text{Ge}}$  antisites and neighboring regular Mn atoms are found to be ferromagnetic and thus provide a possible route toward ferromagnetism. We studied these antisites in 16 atom and 64 atom supercells. We note, however, that in the former case this corresponds to a layer of MnP. Precipitates of MnP have also been invoked as a source of ferromagnetism in this system [14] but would differ from the pure model by adopting a different local crystal structure.

To complete our study, the optical dielectric function is calculated in the AFM and FM states using the Bethe-Salpeter equation (BSE) approach and shows significant excitonic effects.

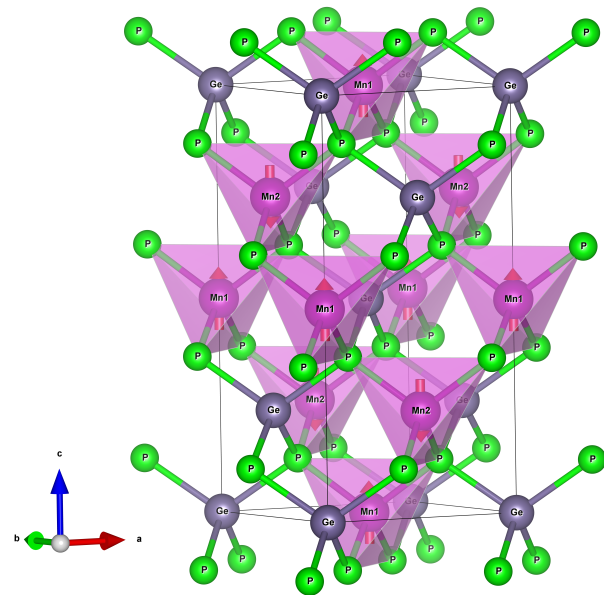


Fig. 1: (a) Crystal structure of the conventional cell with the AFM spin arrangements on the Mn sites in pink, along with Ge sites in gray and P sites in green.

## II. COMPUTATIONAL METHODS

### A. Quasiparticle self-consistent $GW$ method

The calculations are performed using the QUESTAAL suite of codes which implements both DFT and MBPT using a full-potential linear muffin-tin orbital (FP-LMTO) basis set [23]. The QSGW method is a variant of the  $GW$  approach in which an improved non-local (but energy independent) exchange correlation potential  $\tilde{\Sigma}_{xc}$  is extracted from the dynamic (*i.e.* energy-dependent) self-energy,  $\Sigma(\omega)$  as follows

$$\tilde{\Sigma}_{xc} = \frac{1}{2} \Re \left\{ \sum_{nm} |\psi_n\rangle [\Sigma_{nm}(\epsilon_n) + \Sigma_{nm}(\epsilon_m)] \langle \psi_m| \right\}, \quad (1)$$

in which  $\Re$  stands for Hermitian part and  $|\psi_n\rangle$  are the eigenstates of the  $H^0$  Hamiltonian. For details of the justification of this approach see [16, 24]. Thus, instead of making the Green's function  $G$  itself self-consistent, it adjusts the  $G^0$  corresponding to the “non-interacting” Hamiltonian  $H^0$  from which  $\Sigma(\omega) = iG^0W^0$  is calculated by first-order perturbation theory. When  $\tilde{\Sigma}_{xc}$  is iterated to self-consistency, the method becomes independent of the DFT starting  $H^0$  and the quasiparticle energies equal the Kohn-Sham eigenvalues of  $H^0$ . Thus, the method focuses on obtaining the real part of the quasiparticle excitation energies or band structure, rather than the full dynamic self-energy or quasiparticle lifetimes. Optical dielectric functions are calculated using the BSE which was recently implemented in the QUESTAAL suite of codes, as well as a way to go beyond the random phase approxi-

mation (RPA) in the screening of  $W$  by incorporating electron-hole effects, which is then called  $\hat{W}$ . [25, 26]. Details of the QSGW implementation can be found in [16]. Its hallmark is the use of a mixed-product basis set to represent two-particle quantities, an approach which was first introduced by Aryasetiawan and Gunnarsson [27]. Its advantage lies in the use of products of highly accurate numerical radial function times spherical harmonic basis functions or partial waves inside the muffin-tin spheres to represent the short-range screening response. This is easier to converge than a plane-wave representation and also requires fewer high-energy unoccupied bands. The basis set used here was tested for convergence and consists of *spdfspd* functions including Ge-3d local orbitals.

## B. Magnetic Susceptibility and Heisenberg Exchange Interactions

To determine the magnetic ground state, the critical temperature and the low energy excitations (spin waves), one usually starts from a Heisenberg-type spin-Hamiltonian, with the exchange interaction parameters determined from first-principles calculations. The latter can be obtained in various ways. The first of those is to map the total energy differences of various magnetic configurations calculated within spin-dependent DFT to a Heisenberg type spin Hamiltonian with a predetermined extent of the interactions and number of independent exchange interaction parameters. The second approach is to use linear response around a chosen reference spin configuration. This approach has mostly been used in the context of the multiple scattering or Green's function description of the underlying spin-dependent electronic structure and estimates the first-order corrections to the total energy to a static infinitesimal rotation of the spins within each muffin-tin sphere [28]. The generalization of this approach in many-body perturbation theory is to calculate the dynamic transverse spin susceptibility [29]. The spin wave (SW) energies are then in principle obtained from the poles of this transverse spin susceptibility, which one can either calculate in the bare or the interacting limit and Heisenberg type exchange interactions can still be obtained from a static limit. The dynamic spin susceptibility furthermore contains information on the lifetime of the SW excitations.

Here, we use the latter approach in the framework of the QSGW method. This linear response approach starts from the transverse spin susceptibility,  $\chi_{\mathbf{q}}^{0+-}(\mathbf{r}, \mathbf{r}', \omega)$ , expressed in terms of the QSGW wave functions and energy

levels,

$$\begin{aligned} \chi_{\mathbf{q}}^{0+-}(\mathbf{r}, \mathbf{r}', \omega) = & \sum_{\mathbf{k}n\downarrow}^{occ.} \sum_{\mathbf{k}'n'\uparrow}^{unocc.} \frac{\Psi_{\mathbf{k}n\downarrow}^*(\mathbf{r})\Psi_{\mathbf{k}'n'\uparrow}(\mathbf{r})\Psi_{\mathbf{k}'n'\uparrow}^*(\mathbf{r}')\Psi_{\mathbf{k}n\downarrow}(\mathbf{r}')}{\omega - (\epsilon_{\mathbf{k}'n'\uparrow} - \epsilon_{\mathbf{k}n\downarrow}) + i\delta} \\ & + \sum_{\mathbf{k}n\downarrow}^{unocc.} \sum_{\mathbf{k}'n'\uparrow}^{occ.} \frac{\Psi_{\mathbf{k}n\downarrow}^*(\mathbf{r})\Psi_{\mathbf{k}'n'\uparrow}(\mathbf{r})\Psi_{\mathbf{k}'n'\uparrow}^*(\mathbf{r}')\Psi_{\mathbf{k}n\downarrow}(\mathbf{r}')}{-\omega - (\epsilon_{\mathbf{k}n\downarrow} - \epsilon_{\mathbf{k}'n'\uparrow}) + i\delta}, \end{aligned} \quad (2)$$

where  $\mathbf{k}' = \mathbf{k} + \mathbf{q}$ , and  $\Psi$ 's and  $\epsilon$ 's are the spin-dependent band structure eigenstates and eigenvalues, which in our case are calculated in the QSGW approximation. From it, a coarse-grained version between magnetic sites,  $\chi_{ij}^{0+-}(\mathbf{q}, \omega)$ , is obtained by a projection onto the spheres within a rigid spin approximation. Here the indices  $i, j$  refer to sites in the unit cell. Its inverse at  $\omega = 0$  was shown to be related to the Heisenberg exchange interactions  $J_{ij}(\mathbf{q})$  in [19]. The details of how the coarse-graining is carried out can be found in [19]. By an inverse Bloch sum or discrete Fourier transform we extract the real space  $J_{ij}^{0\mathbf{T}}$  between atoms  $i$  in the unit cell at the origin and site  $j$  in the unit cell at the lattice translation vector  $\mathbf{T}$ . Analyzing the corresponding Heisenberg Hamiltonian, we can then calculate the critical temperature in the mean-field or other approximations and also study the spin waves. The mean-field estimate of the critical temperature is typically used as a starting point for the self-consistent iterative process of the RPA scheme, first developed by Tyablikov *et al.* [20] and Callen [21]. The mean-field estimate value is shown to be an upper limit of the RPA value by Rusz *et al.* [22].

We note that in this paper, we concentrate on the collinear magnetic ordering (FM and AFM) within the unit cell of  $I42d$  MnGeP<sub>2</sub>, without including the effects of spin-orbit coupling (SOC). The Mn atoms are the dominant magnetic sites in the structure. When the SOC is neglected, it is indeed the above mentioned spin susceptibility which determines the fundamental magnetic linear response.

To obtain the SW dispersions within the Heisenberg model, we still only need the static and bare spin-susceptibility. However, Kotani and van Schilfhaarde [19] also proposed a way to obtain the interacting spin susceptibility under the assumption that the interaction is wavevector-independent and on-site diagonal. The resulting interacting and transverse dynamic spin-susceptibility but still within a rigid-spin within sites framework contains additional information on the lifetime of the spin-waves and is calculated from

$$\begin{aligned} [D(\mathbf{q}, \omega)]^{-1} = & [D^0(\mathbf{q}, \omega)]^{-1} + \frac{\omega}{M_a} \delta_{aa'} \\ & - M_a^{-1} \sum_b M_b [D^0(\mathbf{q} = 0, \omega)]_{ba}^{-1} \delta_{aa'}, \end{aligned} \quad (3)$$

where  $M_a$  is the magnetic moment of site  $a$  and the  $\mathbf{D}$  and  $\mathbf{D}^0$  are the site versions of the transverse spin susceptibility.

### C. Néel Temperature

We use both the mean-field and random phase approximations (RPA) to estimate the critical (Néel) temperature of antiferromagnetic MnGeP<sub>2</sub>. For a system with various magnetic sites per unit cell, the mean-field critical temperature is calculated by considering the coupled system of equations,

$$\langle s_i \rangle = \frac{2}{3k_B T} \sum_j J_{ij} \langle s_j \rangle, \quad (4)$$

where the  $\langle s_j \rangle$  vector is the average  $z$ -component of the unit vector,  $\langle s_j^{\mathbf{R}} \rangle$ , pointing in the direction of the magnetic moment of the  $j$  atom, located at site  $\mathbf{R}$  within the unit cell. Thus, the mean-field critical temperature is obtained by solving the eigenvalue problem,

$$\left[ \frac{2}{3k_B} J_{ij} - T \mathbf{I} \right] \langle s_i \rangle = 0, \quad (5)$$

whose largest eigenvalue  $T_c$  gives the critical temperature and where  $\mathbf{I}$  is the unit matrix. Here

$$J_{ij} = \sum_{\mathbf{T}} J_{ij}^{\mathbf{0T}} \quad (6)$$

and the sum excludes the on-site term,  $J_{ii}^{\mathbf{00}}$  when  $i = j$  [30].

The mean-field estimate of the critical temperature is typically used as a starting point for the self-consistent iterative process of the RPA scheme, [20, 21].

### D. Optical Dielectric Function

The optical dielectric function is calculated using both the *independent (quasi)particle approximation* and the Bethe Salpeter equation in the Tamm-Damcoff approximation and with static  $W$  [31] as implemented by Cunningham *et al.* [26] in LMTO basis set within the QUESTAAL suite. In the independent particle method, we find the imaginary part of the dielectric function,  $\varepsilon_2$ , by considering the transitions (direct) between the quasiparticle states  $\Psi_i$  with energies  $\epsilon_i$  in the spin polarized  $GW$ :

$$\varepsilon_2(\omega) = \frac{8\pi^2}{\Omega\omega^2} \sum_{c\mathbf{v}\mathbf{k}} |\langle \Psi_{v\mathbf{k}} | \mathbf{e} \cdot \mathbf{v} | \Psi_{c\mathbf{k}} \rangle|^2 \delta(\epsilon_{c\mathbf{k}} - \epsilon_{v\mathbf{k}} - \omega), \quad (7)$$

where  $\Omega$  is the unit cell volume,  $\mathbf{e}$  the polarization and  $\mathbf{v}$  the velocity operator. Since the QSGW equation contains a non-local exchange correlation part, this includes a contribution from  $[\tilde{\Sigma}_{xc}, \mathbf{r}]$ . The integration can here be done using the tetrahedron method and using a fine  $\mathbf{k}$ -mesh.

In the BSE in the Tamm-Dankoff approximation,[31–34] on the other hand, the dielectric function is calculated from the eigenvalues and eigenvectors of a two-particle Hamiltonian which includes the electron-hole

interactions kernel, which mixes up the above vertical transitions between valence and conduction band states ( $\epsilon_{c\mathbf{k}} - \epsilon_{v\mathbf{k}}$ ) at different  $\mathbf{k}$ . The implementation in terms of the LMTO basis set involves the same product basis set also used for the QSGW method following [25, 26]. For a spin-polarized case our calculation includes only transitions between equal spins and neglects the coupling between opposite spin transitions, which, in principle can arise from the exchange part of the kernel. [34] Also, we note that our calculation does not include indirect band to band transitions facilitated by electron-phonon coupling.

## III. RESULTS

The chalcopyrite crystal structure is shown in Fig.1. It belong to the spacegroup number 122,  $I42d$  or  $D_{2d}^{12}$ . The conventional body centered cell contains 16 atoms, but we use the primitive cell of 8 atoms. The labeling of the Mn atoms in this figure corresponds to the antiferromagnetic ordering as detailed later. The conventional unit cell's lattice parameters are  $a = 5.453 \text{ \AA}$  and  $c = 10.780 \text{ \AA}$  with the ratio  $c/a = 1.977$ . The Wyckoff positions are: Ge,  $4a$  (0, 1/2, 1/4), Mn  $4b$  (1/2, 0, 1/4) and P  $8d$  (3/4, 3/8, 3/8) with  $u = 0.255137$  the only internal structural parameter which is not fixed by symmetry. Because the system is body centered, we can use a 8 atom cell with  $\mathbf{a}_1 = (-1/2, 1/2, 1/2)$ ,  $\mathbf{a}_2 = (1/2, -1/2, 1/2)$ ,  $\mathbf{a}_3 = (1/2, 1/2, 1/2)$  in terms of the lattice vectors of the conventional cell. The labeling of high symmetry points in the Brillouin zone follows the notation of the Bilbao Crystallographic Server, <https://www.cryst.ehu.es/>.

### A. Band Structures

The Mn- $d$  state spin-polarization plays an essential role in making the band structure insulating. Without it, the partially filled  $d$  states of Mn would lie at the Fermi level and there would be no band gap. To create a suitable starting point for the ferromagnetic QSGW calculations, we use the DFT+ $U$  approach. The effect of adding a Hubbard- $U$  is to shift down occupied  $d$ -states on Mn by  $\sim U/2$  and empty  $d$ -states up. This reduces the hybridization of the occupied Mn- $d$  states with the P- $p$  states in the occupied bands, which then dominate the valence band maximum (VBM). Likewise, the empty Mn- $d$  states are interacting less with the Ge- $s$  states, which becomes the conduction band minimum (CBM). A small gap opens up depending on the choice of  $U$ . Starting from the Green's function  $G^0$  of this DFT+ $U$  band structure, we then calculate the self-energy  $\tilde{\Sigma}_{xc}^0$ . From here on, we switch off the  $U$  and let the self-energy  $\tilde{\Sigma}_{xc}$  evolve to self-consistency. Essentially the self-energy takes over the role of the  $U$ . Using the same approach we calculate both the FM and AFM band structures and we also use both the original QSGW method in which  $W$  is calcu-

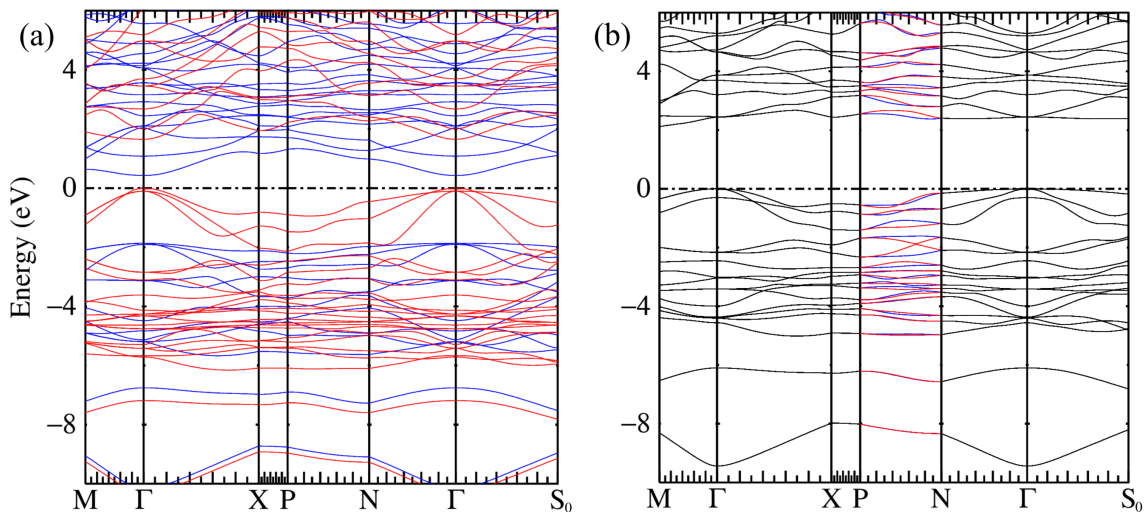


Fig. 2: Band structure of  $\text{MnGeP}_2$  obtained in the  $\text{QSG}\hat{W}$  approach. Majority spin (red), minority spin (blue). The Fermi energies are shifted to zero. (a) FM and (b) AFM.

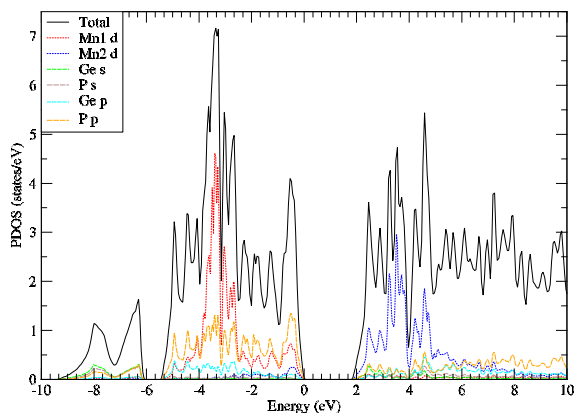


Fig. 3: Total and partial densities of majority spin states in the  $\text{QSG}\hat{W}$  approach for AFM  $I42d$   $\text{MnGeP}_2$ .

The partial contributions include the sum over all equivalent atoms of a given type but refer to partial wave contributions inside the spheres only, excluding contributions from the interstitial region and only show the major contributions.

lated in the random phase approximation (RPA) and in the improved  $\text{QSG}\hat{W}$  method in which the electron-hole interaction effects are included in  $W$ , now labeled  $\hat{W}$ . This approach introduced in [25, 26] has been shown to be equivalent to a vertex correction in the polarization propagator and includes so-called ladder diagrams. The final  $\text{QSG}\hat{W}$  band structures obtained in this way for the FM and AFM cases are shown in Fig. 2 and the band gaps are listed in Table I.

TABLE I: Band gaps in ferromagnetic and antiferromagnetic  $I42d$   $\text{MnGeP}_2$ .

Method	Ordering	$k_v$	$k_c$	Spin	Gap (eV)
$G\hat{W}$	FM	$\Gamma$	$\Gamma$	$\uparrow\downarrow$	0.426
$G\hat{W}$	FM	$\Gamma$	$\Gamma$	$\uparrow\uparrow$	1.653
$G\hat{W}$	FM	$\Gamma$	$\Gamma$	$\downarrow\downarrow$	2.293
$G\hat{W}$	AFM	$\Gamma$	M	all	2.120
$G\hat{W}$	AFM	$\Gamma$	$\Gamma$	all	2.440
$GW$	FM	$\Gamma$	$\Gamma$	$\uparrow\downarrow$	0.634
$GW$	FM	$\Gamma$	$\Gamma$	$\uparrow\uparrow$	1.800
$GW$	FM	$\Gamma$	$\Gamma$	$\downarrow\downarrow$	2.476
$GW$	AFM	$\Gamma$	M	all	2.197
$GW$	AFM	$\Gamma$	$\Gamma$	all	2.488
$GGA + U$	AFM	$\Gamma$	M	all	0.724
$GGA + U$	AFM	$\Gamma$	$\Gamma$	all	0.898

For the FM case, the top of the valence band has majority spin while the lowest conduction bands have minority spin. The majority spin VBM and the CBM of minority spin are both located at  $\Gamma$ , implying a direct but spin forbidden gap. The gaps are all slightly reduced in the  $\text{QSG}\hat{W}$  case which is shown in Fig2(a).

The band structure for the AFM case in which the two atoms in the unit cell have opposite magnetic moments and which is found to have lower total energy within the  $GGA+U$  approximation, is shown in Fig. 2(b). The lowest band gap is now indirect between CBM at  $M$  and VBM at  $\Gamma$ . Its band gaps are included in Table I in both approximations and in the starting  $GGA+U$  method. For the FM case the latter still had a metallic band structure. Interestingly, the lowest direct gap is notably larger in the AFM than the FM case.

The total density of states and its decomposition into partial orbital contributions is shown in Fig. 3 for the AFM case in the QSGW approximation. We can see that the Mn-3d states occur around  $-4$  to  $-2$  eV and spread from 2 to 5.5 eV respectively but the majority spin (occupied) and minority spin bands (empty) occur on the different Mn although overall the total DOS of minority and majority spin are the same as required for an antiferromagnet. The top valence bands have primarily P- $p$  character. The lowest bands near -8 eV have mixed P-3s P-3p character while the mostly P-3s bands occur near -29 eV and are not shown here. They lie close to the Ge-3p semi core states.

Although the band plots in the AFM case show the spin up and spin down bands are degenerate along several symmetry lines, we see a splitting of the bands along  $PN$ . This is a signature of altermagnetism. Indeed, the spacegroup  $I\bar{4}2d$  supports altermagnetism [35]. The symmetry elements that relate the spin-up and spin-down Mn<sub>1</sub> and Mn<sub>2</sub> are generated by the 2-fold rotation about the  $x$  or  $y$  axis. They split the group  $D_{2d}$  into the subgroup  $S_4$  and its coset  $C_{2x}S_4$  containing the elements  $\{C_{2x}, C_{2y}, \sigma_{(110)}, \sigma_{(1\bar{1}0)}\}$ . For any  $\mathbf{k}$  in one of the diagonal mirror-planes, the mirror operation belongs to the little group of  $\mathbf{k}$  and the spin degeneracy is protected [35]. This includes the bands along  $\Gamma M$  and  $\Gamma N$ . Likewise along  $\Gamma X$ , the  $C_{2x}$  operation protects the spin-degeneracy while along  $XP$  it is a combination of time reversal  $\mathcal{T}$  with a two fold rotation  $C_{2y}$  that protects the degeneracy. However along  $SG$  and  $NP$  rather sizable spin splittings are observed. Following the approach of Yuan *et al.* [36], the splittings as function of  $\mathbf{k}$  along the  $SG$  and  $NP$  lines are plotted separately for a few of the bands in Fig. 4. We can see that its maximum is  $\sim 0.35$  eV along the  $NP$  line for the vb9-vb10 splitting counting valence bands down from the top but is also significant for the lowest conduction band (0.2 eV) cb1-cb2 and may thus have impacts on transport properties.

## B. Optical Properties

Absorption or reflectivity or spectroscopic ellipsometry in the visible to ultraviolet range provide a convenient way to probe the band structure via interband transitions. To facilitate future comparisons to experimental work of the interband related optical properties, we have calculated the optical dielectric function both in the independent particle approximation and in the BSE approach, which includes local-field and electron-hole interaction effects. Because the chalcopyrite structure has tetragonal symmetry, the macroscopic dielectric function has two independent components, parallel or perpendicular to the  $\mathbf{c}$ -axis. Optical properties are studied in the AFM case since we find the AFM configuration to be the lowest energy. The results, shown in Fig. 5, are based on the QSGW band structure.

Our calculation includes a fixed broadening factor

which simulates both the lifetime and the spread in  $\mathbf{k}$ -space around the Brillouin zone sampling  $\mathbf{k}$  points. We use a  $5 \times 5 \times 5$  mesh and a broadening parameter of 0.005 Rydberg. The BSE results are also sensitive to the number of valence and conduction bands included in the transitions. Here we include 22 valence and 16 conduction bands. This includes the upper valence band set derived primarily from the 12 P-3p orbitals and the 10 Mn-3d  $\uparrow$  orbitals in the AFM case, which extend down to about  $-5$  eV from the VBM and up to about 8 eV in the conduction band. This should be adequate to obtain  $\varepsilon_2(\omega)$  converged up to about 13 eV.

We can see that the BSE shifts the peaks in  $\varepsilon_2(\omega)$  to lower energy and changes the shape of the spectrum. In other words, it red shifts the oscillator strengths. Examining the eigenvalues of the effective two-particle Hamiltonian, and their relative oscillator strengths, we can see more detail of the lowest excitations without the broadening effects. These are plotted as narrow vertical bars on the same plot but with an arbitrarily adjusted overall scale factor. We can now see that there are in fact bound state excitons below the direct gap of 2.44 eV. We note, however that these all are still lying above the lowest indirect gap of 2.12 eV. Our present calculation does not include indirect contributions which require inclusion of electron-phonon mediated second order processes and are therefore expected to be significantly weaker. We anticipate that there will be also bound state excitons associated with the indirect gap and with similar exciton binding energies. The binding energy of the excitons is sensitive to the  $\mathbf{k}$ -point sampling and requires a finer sampling to be accurate than we can here afford. Furthermore, it would require including the phonon contributions to the screening of the electron-hole interaction, which is beyond the scope of the present paper and would require further study. We therefore refrain from a detailed discussion of the exciton binding energies or exciton spectrum. Here we point out that there are indeed excitons and that on the larger energy scale in the continuum the electron-hole interaction effects are significant. We can also see significant anisotropy between the  $\mathbf{E} \parallel \mathbf{c}$  and  $\mathbf{E} \perp \mathbf{c}$  spectra.

## C. Magnetic Properties

Having established the electronic band structure for both FM and AFM cases, we now turn to the question of magnetic ordering in the perfect crystal. The calculations of magnetic properties in this section is based on the QSGW underlying electronic structure. We label the exchange interactions  $J_{ij}^{\mathbf{T}}$  between atom number  $i$  in the unit cell centered at the origin and  $j$  in the unit cell with lattice vector  $\mathbf{T} = n_1 a\hat{\mathbf{x}} + n_2 a\hat{\mathbf{y}} + n_3 c\hat{\mathbf{z}}$  denoted as  $(n_1, n_2, n_3)$  in Table II. In other words, the lattice vectors here are given in reduced coordinates of the conventional cell. The table lists just a few of the larger interactions and the total cumulative sum. The dependence of these

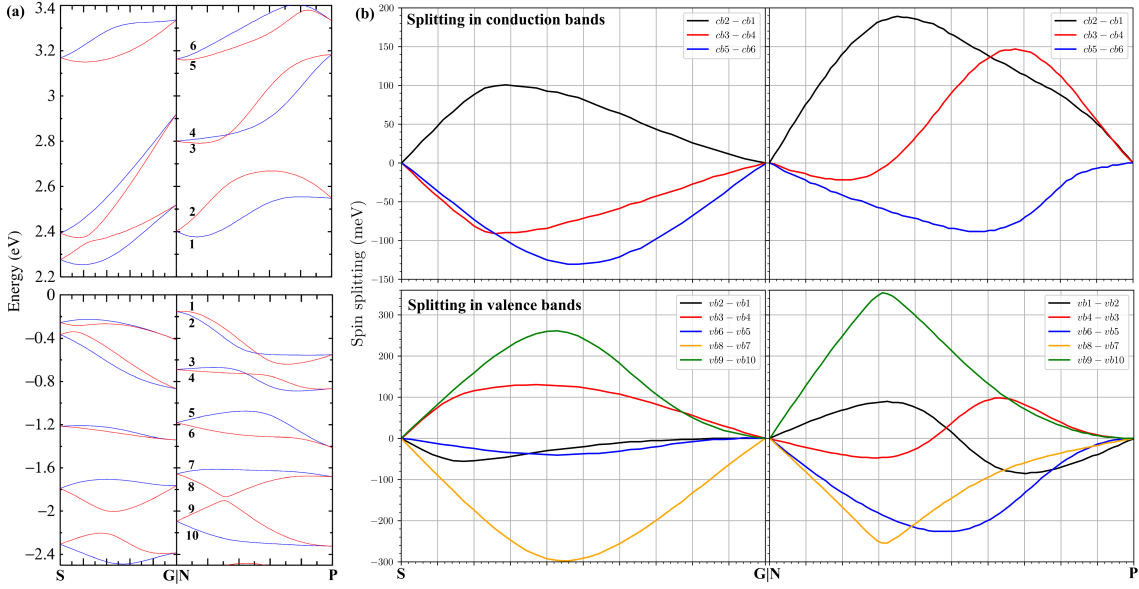


Fig. 4: (a) Conduction and valence bands obtained in the  $\hat{G}\hat{W}$  level along the symmetry lines where major splittings occur. Majority spin (red), minority spin (blue) (b) Differences of majority minus the minority energies in successive bands.

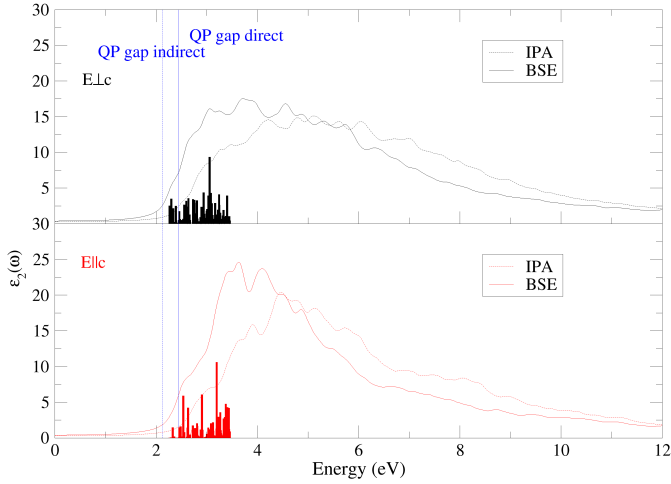


Fig. 5:  $\epsilon_2(\omega)$  and oscillator strengths obtained within the Bethe-Salpeter and independent particle approximation schemes applied in the  $\hat{G}\hat{W}$  level.

exchange interactions on distance is shown in Fig. 6. We can see that apart from the nearest neighbor interactions they quickly converge to almost zero with some minor oscillations. We find that the major interaction is  $J_{12}^{(0,0,0)}$ , which is the nearest neighbor interaction between the  $Mn_1$  and  $Mn_2$  sites in the same primitive cell, as shown in Fig. 1(a)), and is negative for both FM and AFM reference calculations. This shows clearly that pure  $MnGeP_2$  is predicted to be AFM confirming various previous DFT studies[10, 11]. On the other hand we find the exchange interactions in the (001) planes to be very weakly an-

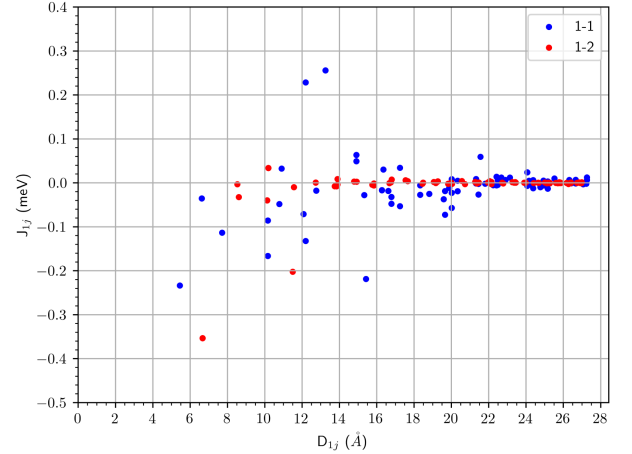


Fig. 6: Exchange interactions  $J_{11}^T$  and  $J_{12}^T$  as function of distance  $|\tau_i - \tau_j - \mathbf{T}|$  from the AFM ordering. The nearest neighbor  $J_{12}^{(0,0,0)}$  is left off as it is much larger in absolute value from the other ones.

tiferromagnetic,  $J_{11}^{(100)} = -0.017$  and  $J_{11}^{(110)} = -0.008$ . Besides the clear antiferromagnetic ordering between adjacent (001) planes, this suggests there could be a further antiferromagnetic checkerboard ordering pattern in these planes but these interactions are about two orders of magnitude smaller.

The primitive AFM cell calculation yielded converged magnetic moments of  $Mn_1$  and  $Mn_2$  to be  $\pm 4.576\mu_B$ , with zero net magnetic moment, whereas in the FM calculation, each site's magnetic moment is found to be  $4.812\mu_B$ , with a net moment of  $10\mu_B$  including the small

TABLE II: Exchange interactions based on FM or AFM reference state;  $i$  and  $j$  label the magnetic atom site numbers in the primitive cell, and  $\mathbf{T}$  gives the lattice vector in units of the conventional cell lattice vectors,  $n^*$  is the number of equivalent neighbors in the star,  $J_{ij}^{\mathbf{T}}$  is the exchange interaction in mRy, and  $\sum_{\mathbf{T}} J_{ij}^{\mathbf{T}}$  is the cumulative sum up to  $|\tau_i - \tau_j - \mathbf{T}| < r_{cut} = 5a$

Ordering	i	j	$n^*$	$\mathbf{T}$	$J_{ij}^{\mathbf{T}}$	$\sum_{\mathbf{T}} J_{ij}^{\mathbf{T}}$
FM	1	1	4	(-1,0,0)	-0.01956	-0.078
FM	1	1	4	(1, 1, 0)	-0.0282	-0.257
FM	1	1	2	(0, 0, 1)	0.0122	-0.353
FM	1	1		all		-0.452
FM	1	2	4	(0, 0, 0)	-0.93197	-3.728
FM	1	2	8	(-1, 0, 0)	-0.0515	-4.14
FM	1	2		all		-3.922
AFM	1	1	4	(-1,0,0)	-0.01717	-0.069
AFM	1	1	4	(1,1,0)	-0.01608	-0.157
AFM	1	1		all		-0.356
AFM	1	2	4	(0,0,0)	-1.01882	-4.075
AFM	1	2	8	(-1,0,0)	-0.026	-4.283
AFM	1	2	4	(-1, 0, 1)	-0.01487	-4.357
AFM	1	1		all		-4.359

contributions from the Ge- $d$  and P- $d$  orbitals and interstitial contributions. These magnetic moments correspond closely to  $S = 5/2$  as expected for  $\text{Mn}^{2+}$ . In the approach of Kotani and van Schilfhaarde [19] the spin of the Heisenberg model is set to  $M_i = 2S_i$ .

We can see that the dominant exchange interaction is between the closest site 1 and site 2 Mn and is about  $-1$  mRy with a slightly higher absolute value in the AFM case than in the FM reference case. All other interactions are at least 2 orders of magnitude smaller. Each  $\text{Mn}_1$  has 4 nearest neighbor  $\text{Mn}_2$  atoms in the primitive cell in the adjacent layers in the  $c$ -direction. If we ignore all other interactions, the mean field  $T_c$  would be  $(2/3)N J_{12}^{nn}$ , with  $N$  the number of nearest neighbors within a classical Heisenberg model with unit vectors as spins and gives an estimated mean field temperature of 428 K. Correcting this by a quantum correction factor of  $S(S+1)/S^2 \approx 1.4$  we would obtain  $T_N^{MF} \approx 600$  K. This is an overestimate because of the mean field approximation. We may compare to the case of MnO in [19]. In that case the authors found that the  $T_N$  already agreed reasonably well with experiment even without the quantum correction.

A more accurate calculation of the critical temperature is obtained using the approach described in Sec. II C and is used as starting point for the Tyablikov method. The Tyablikov method is sensitive to the  $\mathbf{k}$ -point sampling and may converge to different fixed points. Using up to a  $13 \times 13 \times 13$  mesh we obtain a converged Néel tempera-

ture of 423 K in the mean field approximation and  $176 \pm 2$  K in the Tyablikov method. Multiplying the RPA estimate by a quantum correction as mentioned before would yield about 246 K. At present we have no experimental data on AFM  $\text{MnGeP}_2$  as all samples yield ferromagnetic behavior for reasons to be discussed in later sections.

We next turn our attention to the spin waves which, in principle, could provide a more direct test of the exchange interactions, although unfortunately no such data are presently available. Fig. 7 shows the spin wave energies  $\omega(\mathbf{q})$  of the pure crystal obtained from

$$\det \left\{ \omega(\mathbf{q}) \delta_{ij} \frac{1}{S_i} - \frac{1}{S_i} \tilde{J}_{ij}^{\mathcal{H}}(\mathbf{q}) \frac{1}{S_j} \right\} = 0 \quad (8)$$

with

$$\tilde{J}_{ij}^{\mathcal{H}}(\mathbf{q}) = J_{ij}^{\mathcal{H}}(\mathbf{q}) - \delta_{ij} \frac{1}{S_i} \left( \sum_{\mathbf{k}} J_{ik}^{\mathcal{H}}(\mathbf{q} = 0) S_k \right) \quad (9)$$

with  $2S_i = M_i$  and the  $J_{ij}^{\mathcal{H}}(\mathbf{q}) = [D^0(\mathbf{q}, \omega = 0)]^{-1}$  of Eq. (3) apart from the on-site terms. Within the simplified model of only one nearest neighbor interaction  $J_{12}$  we can obtain the spin wave energy analytically as

$$\omega(\mathbf{q}) = |J_{12}| \sqrt{z^2 - \left( \sum_{\mathbf{d}} e^{i\mathbf{q} \cdot \mathbf{d}} \right)^2} \quad (10)$$

with  $z$  the number of nearest neighbors, which in our case is 4 and the sum over neighbors amounts to

$$\sum_{\mathbf{d}} e^{i\mathbf{q} \cdot \mathbf{d}} = 2 \cos(k_x a/2) e^{ik_z c/4} + 2 \cos(k_y a/2) e^{-ik_z c/4} \quad (11)$$

which at  $k_X = (0, \pi/a, 0)$  amounts to  $|J_{12}|2\sqrt{3}$  or about 48 meV for  $\omega(\mathbf{q})$ . At  $k_M = (0, 0, \pi/c)$  the spin wave energy is  $|J_{12}|2\sqrt{2}$  or 39 meV and at  $k_N = (\pi/2a, \pi/2a, \pi/2c)$ , it is  $|J_{12}|3.03$  or 42 meV. Thus the maxima in the spinwave spectrum are consistent in order of magnitude with the model of a single dominant exchange interaction between nearest neighbors. A measurement of the spin wave dispersion could directly confirm our exchange interaction estimates.

Besides the spinwave dispersion relation shown as green dashed lines in Fig.7 this figure show the imaginary part of the trace of the  $D(\mathbf{q}, \omega)$  which represents the site averaged dynamic transverse spin susceptibility. The magnitude of this quantity is shown as a color scale as function of  $\mathbf{q}$  and  $\omega$ . We can see that its maximum nicely follows the spin wave energy as expected. We caution that the heatmap color scale is on a logarithmic scale. As a result the width of the spectral function around the actual spin wave energy reflects largely the Lorentzian line shape. In principle, the width of  $\Im \text{Tr}[D(\mathbf{q}, \omega)]$  is the inverse of the lifetime of the collective spinwave excitation, which, physically arises from decay into spin-flip excitations. While in an altermagnet we indeed have small

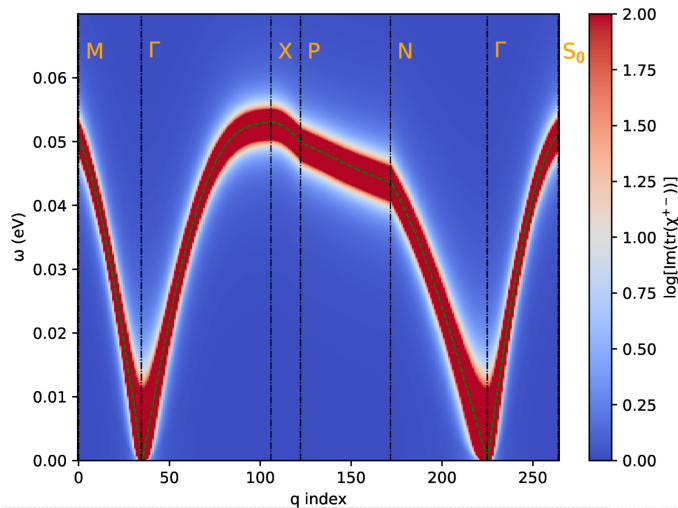


Fig. 7:  $\Im Tr\{\chi^{+-}(\omega)\}$  as color scale and spin wave dispersion,  $\omega(\mathbf{q})$  (green dashed line) for AFM MnGeP<sub>2</sub>.

energy spin splittings in the bands these can only become excited if we first have electron hole pairs excited to the band edges at finite temperature, which is not included here. The smallest spin flip excitations allowed in our calculation are across the band gap and thus provide only negligible width because the electronic band gap is much larger than the spin wave energy maximum.

#### D. Effects of Carrier Doping

Past studies ([12], [13], [14]) on synthesized MnGeP<sub>2</sub> found ferromagnetic hysteresis and resonance. To explain the possible source of ferromagnetism, we first analyze the effect of carrier mediated exchange interactions on the dominant antiferromagnetic exchange interaction, by introducing a simple model for carrier doping. We basically assume a rigid band structure but change the occupation of the valence or conduction bands by adding a positive or a negative homogeneous background charge density to the structure. Introducing a negative background charge simulates the effects of hole doping, since the charge neutrality requires fewer valence electrons. Whereas introducing a positive background simulates electron doping. The resulting dominant interactions under each type of doping are listed in table III.

We can see that both hole or electron doping lowers the absolute value of the relevant exchange interaction and the decrease increases with the doping concentration but is not simply proportional to it. It appears that electron doping is more effective at lowering the antiferromagnetic exchange, but even for the high concentration of dopants simulated here, like 1 electron or hole per unit cell, or about  $5.4 \times 10^{21} \text{ cm}^{-3}$ , the effect is less than 5%.

We conclude that the carrier mediated interactions are not enough to explain the observed ferromagnetism in MnGeP<sub>2</sub>.

TABLE III: Effect of carrier doping by introducing a homogeneous background charge

Charge (e)	$J_{12}$
-1	-0.99976
-0.5	-1.00259
-0.1	-1.01415
0	-1.01882
0.1	-1.00876
0.5	-0.98269
1	-0.95391

#### E. Mn<sub>Ge</sub> anti-site defects

As a second possible source of ferromagnetic interactions, we consider Mn<sub>Ge</sub> antisite defects based on the suggestions of the work of Mahadevan and Zunger [11]. We consider several models. In the first one, we use the 16 atom conventional cell and replace one Ge by a Mn. Effectively this changes the stoichiometry and adds a full layer consisting of MnP. While bulk MnP has a different crystal structure, this model nonetheless simulates in some approximate sense a MnP precipitate but maintaining the tetrahedrally bonded zincblende structure. Note, that we are not claiming the existence of such a monolayer type precipitate. Rather, we are exploring the qualitative effect of adding Mn on Ge sites. In this model, the mean-field critical temperature estimate is 560.4 K and the RPA estimate is 390.9 K. See Fig. 8 and table IV for the detailed tabulations of the exchange interactions between the antisite Mn and the other Mn within the structure.

We can see that all of the exchange interactions between the Mn<sub>Ge</sub> antisite with regular Mn are ferromagnetic with  $J_{51}^0$  being the strongest interaction. It is in fact stronger by an order of magnitude than the other ones even though it is not the nearest neighbor. The  $J_{52}^0 = J_{54}^{(0,0,-1)}$  corresponds to a slightly shorter distance because of the  $c/a < 2$  but is between opposite spins in the reference structure. The exchange interaction between two Mn<sub>Ge</sub>,  $J_{55}$  are also ferromagnetic and strongest for the (1,1,0) direction. Meanwhile, the exchange interactions between the regular Mn atoms on Mn sites stay antiferromagnetic between near neighbor layers but are weaker for the Mn in the plane of the Mn<sub>Ge</sub>.

The reference spin configuration studied here has a net surplus of spin up over spin down Mn and is thus ferromagnetic. However, the presence of ferromagnetic coupling to the neighboring Mn even the ones of opposite spin in the reference indicates that the reference system used may not be the ground state. It is clear that all the Mn in the MnP plane have ferromagnetic coupling. As for the net coupling between the adjacent layers, like Mn<sub>3</sub>, these atoms have ferromagnetic coupling with two

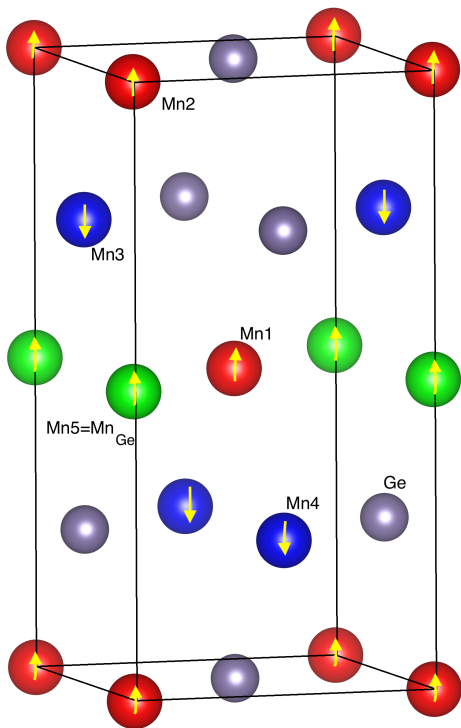


Fig. 8: Labeling of the Mn atoms and assumed spin configuration in the 16 atom conventional cell with  $\text{Mn}_{\text{Ge}}$  antisite. Mn atoms with spin-up are shown in red and Mn atoms with spin-down are shown in blue. Ge are gray and P atoms are not shown. The green sphere is the  $\text{Mn}_{\text{Ge}}$  antisites is assigned to up spin. The  $\text{Mn}_4$  atoms nearest to  $\text{Mn}_5$  correspond to  $\mathbf{T} = (0, 0, -1)$ .

TABLE IV: Exchange interactions involving  $\text{Mn}_{\text{Ge}}$  in 16 atom cell. The atom labeling is shown in 8.  $\text{Mn}_1$  ( $\boldsymbol{\tau}_1 = (1/2, 1/2, 0)$  in reduced coordinates) and  $\text{Mn}_3$  ( $\boldsymbol{\tau}_3 = (0, 0, 1/2)$ ) are  $\uparrow$ -spin,  $\text{Mn}_2$  ( $\boldsymbol{\tau}_2 = (1/2, 0, 1/4)$ ) and  $\text{Mn}_4$  ( $\boldsymbol{\tau}_4 = (0, 1/2, 3/4)$ ) are  $\downarrow$ -spin and  $\text{Mn}_5$  is the  $\text{Mn}_{\text{Ge}}$  with  $\uparrow$ -spin;  $\mathbf{T}$  gives lattice translation vectors,  $|\mathbf{R}| = |\boldsymbol{\tau}_j - \boldsymbol{\tau}_i + \mathbf{T}|$  in  $\text{\AA}$ ,  $N_j$  the number of equivalent neighbors and  $J_{ij}^{\mathbf{T}}$  gives the exchange interaction in mRy.

i	j	$\mathbf{T}$	$ \mathbf{R} $	$N_j$	$J_{ij}^{\mathbf{T}}$
5	1	(0,0,0)	3.856	4	1.155
5	3	(0,0,0)	3.834	2	0.118
5	4	(0,0,-1)	3.834	2	0.118
5	2	(0,0,0)	5.390	2	0.128
5	4	(0,0,0)	8.533	4	0.045
5	5	(1,0,0)	5.453	4	0.041
5	5	(1,1,0)	8.811	4	0.248
5	5	(0,0,1)	10.780	2	-0.010
1	3	(0,0,0)	3.834	2	-0.482
1	4	(0,0,-1)	3.834	2	-0.482
2	3	(0,0,0)	3.834	2	-0.820
2	4	(0,0,0)	3.834	2	-0.820

$\text{Mn}_5$  but still stronger antiferromagnetic coupling to the two  $\text{Mn}_1$  and even stronger antiferromagnetic coupling with the atoms in the next  $\text{Mn}_2$  spin-up layer. It thus appears that the overall antiferromagnetic ordering of alternating spins along the  $[001]$  direction is compatible with the exchange interactions found and would be maintained. To test this, a ferromagnetic alignment of all Mn in this cell was calculated and found to have higher energy in the GGA+U model than the AFM configuration.

Adding this MnP layer, the system also becomes metallic. Indeed, the band structure for this 16 atom cell is shown in Fig. 9 (a) and shows the Fermi level crossing through the majority spin bands. Qualitatively this agrees with the observation of metallic behavior in samples of  $\text{MnGeP}_2$  in which direct evidence was obtained for MnP clusters and for ferromagnetic resonance [9]. Although our model does not faithfully represent actual MnP structure precipitates but rather a single layer of tetrahedrally bonded MnP inserted in the otherwise AFM structure, it shows that inserting MnP can make the system ferrimagnetic and metallic. The Curie critical temperature in our model is higher than the observed ones and we expect that quantum corrections might still further increase it. Actual MnP has a  $T_C = 291$  K close to the observed ferromagnetic temperature in  $\text{MnGeP}_2$  samples which were shown to contain MnP precipitates [14]. From the above analysis, it appears that merely inserting a layer of MnP as in our model is not sufficient to make the overall system ferromagnetic. The occurrence of a metallic band structure might induce longer range carrier mediated exchange couplings, but in principle these are already included in our model as the exchange interactions are obtained from the electronic structure. This suggests that to obtain ferromagnetic behavior, larger cluster of actual MnP structure may be required to form as a true secondary phase.

In the above model we broke the overall stoichiometry by adding net Mn. We also studied a 16 atom cell in which the  $\text{Mn}_{\text{Ge}}$  is compensated by a nearby  $\text{Ge}_{\text{Mn}}$ , in other words we create a exchange defect by swapping a Mn and a Ge instead of adding Mn. In that case, we find that the  $J_{53} = -1.393$  of the  $\text{Mn}_{\text{Ge}}$  with its nearest neighbor layers is antiferromagnetic. The exchange interactions between adjacent layer Mn, such as  $J_{23} = J_{24} = -1.087$  also stay antiferromagnetic while the  $J_{25} = -0.075$  becomes weakly antiferromagnetic. This again suggests that the AFM ordering of adjacent (001) planes is maintained as in the perfect crystal. There is in this case also a weak  $J_{55}^{(110)} = -0.138$  antiferromagnetic coupling and also  $J_{55}^{(100)} = -0.060$  coupling, suggesting that in the basal plane antiferromagnetic ordering of the  $\text{Mn}_{\text{Ge}}$  could be favored in a checkerboard pattern doubling the unit cell in two directions. But we should recall that this model of just swapping a Mn and Ge in the basal plane itself is somewhat artificial in the first place.

Next we consider whether more isolated  $\text{Mn}_{\text{Ge}}$  may already introduce ferromagnetic couplings and metallicity. In this model, we start from the conventional AFM cell,

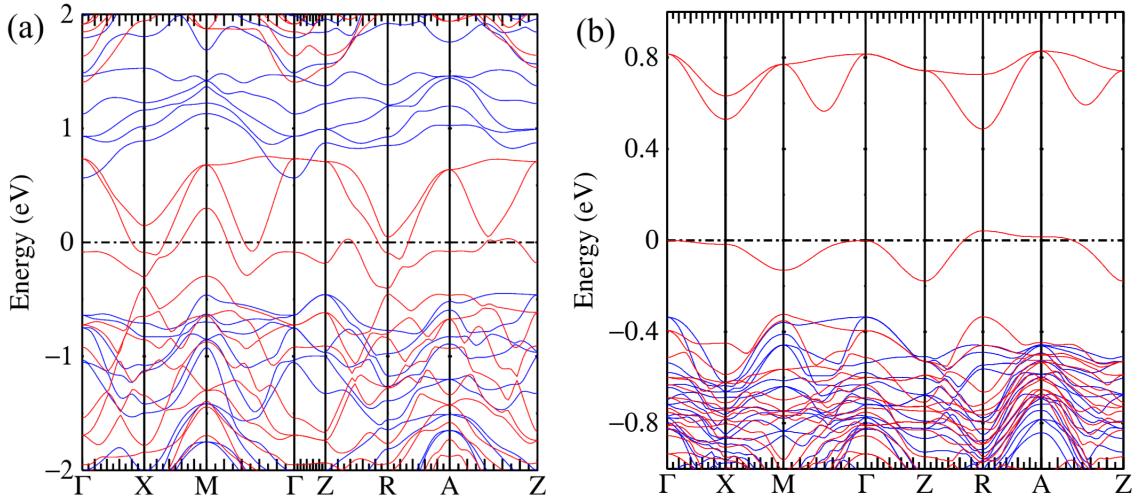


Fig. 9: Band structures of the (a) 16 atom cell and (b) 64 atom cell obtained in the QSGW approach. Majority spin (red), minority spin (blue). The Fermi energy is shifted to zero.

double it in the  $x$  and  $y$  direction and then replace one Ge by a Mn. The converged magnetic moments keep their spin direction and are about  $\pm 4.6 \mu_B$  on the regular Mn and  $3.4 \mu_B$  on the antisite. The strongest interaction of the  $\text{Mn}_{\text{Ge}}$  is again with its nearest neighbor regular Mn of the same spin and in the same basal plane at a distance of  $3.856 \text{ \AA}$ , and is ferromagnetic with a value of  $1.309 \text{ mRy}$ . The other interactions with near neighbors of opposite spin in the reference structure in the layers just above and below are  $0.221 \text{ mRy}$ . The interactions with like spin atoms at a distance of  $7.667 \text{ \AA}$  are  $0.103 \text{ mRy}$ . These are somewhat larger than in the 16 atom cell but still of similar magnitude. The  $\text{Mn}_{\text{Ge}}\text{-Mn}_{\text{Ge}}$  are farther away and their interactions become negligible, indicating that we approach the isolated defect limit. Since we have net more spin up than spin down Mn the overall system in the reference state calculated here is strictly speaking ferrimagnetic. In this model, the mean-field estimate of the critical temperature is  $419.1 \text{ K}$  and the RPA estimate is  $256.1 \text{ K}$ . The band structure shown in Fig. 9 (b) shows a partially filled defect band in the gap which also indicates possibly metallic behavior by hole carriers. As in the 16 atom cell, the nearest neighbor Mn around each  $\text{Mn}_{\text{Ge}}$  have ferromagnetic interactions, which indicates that a cluster of parallel spins may form. However, the exchange interactions between near neighbor regular Mn site atoms in adjacent basal planes stays antiferromagnetic and range from  $-0.67$  to  $-0.996 \text{ mRy}$ . This indicates that the host  $\text{MnGeP}_2$  maintains an antiferromagnetic ordering in which the small clusters of parallel spin around each  $\text{Mn}_{\text{Ge}}$  are embedded. Depending on the concentration of  $\text{Mn}_{\text{Ge}}$  antisites and whether we are above or below the percolation threshold the system may overall become ferromagnetic in the same way as a dilute magnetic semiconductor.

In summary of this section the presence of  $\text{Mn}_{\text{Ge}}$  antisites is found to lead to ferromagnetic coupling between

these antisite Mn and the near neighbor regular Mn atoms in the system. This conclusion agrees with the findings of Mahadevan and Zunger[11]. This indicates that Mn-rich  $\text{MnGeP}_2$  can behave ferrimagnetic. Our calculations do not allow us to decide whether the observed ferromagnetic properties of actual  $\text{MnGeP}_2$  samples results simply from a sufficient concentration of such antisite defects or the presence of actual MnP precipitates with their own crystal structure and sufficient size to establish a separate ferromagnetic phase inside an antiferromagnetic host. However, our detailed analysis indicated that merely inserting a layer of MnP would not be sufficient to break the overall antiferromagnetic ordering between adjacent (001) planes. Also, if the  $\text{Mn}_{\text{Ge}}$  are compensated by  $\text{Ge}_{\text{Mn}}$  at nearby sites, we find predominantly antiferromagnetic couplings and the AFM order is preserved.

Under certain growth conditions, the occurrence of MnP as a secondary phase was established by X-ray diffraction, [14] indicating that these precipitates were large enough and these samples showed ferromagnetic resonance with a Curie temperature close to that of the known  $T_C$  of bulk MnP. This does not preclude that other mechanisms for ferri or ferromagnetism could occur under different crystal growth conditions closer to ideal  $\text{MnGeP}_2$ . On the other hand it may be difficult to avoid low energy exchange defect or slight deviations from stoichiometry altogether as these defects have a fairly low energy of formation. But while adding  $\text{Mn}_{\text{Ge}}$  produces some ferromagnetic couplings near them, they are also insufficient to change the overall system into a ferromagnet but rather to a ferrimagnet. Our calculations suggest the formation of parallel spin clusters near  $\text{Mn}_{\text{Ge}}$  antisites embedded in an overall antiferromagnetic host.

#### IV. CONCLUSIONS

In this paper we studied the electronic structure and the derived interband optical transition and magnetic properties of chalcopyrite  $\text{MnGeP}_2$  using the QSGW approach. In agreement with previous DFT work, we found an antiferromagnetic ground state. We determined the band structure and optical dielectric function using the QSGW variant of the method in which electron-hole effects are included in the screening of  $\hat{W}$ . We find an indirect band gap of about 2.12 eV and lowest direct gap of 2.44 eV and significant excitonic effects. We also found that in a ferromagnetic configuration the gap is significantly smaller and direct. Interestingly, the antiferromagnetic structure is actually an altermagnet, showing spin splittings of the bands along certain  $\mathbf{k}$ -lines. This is because the two magnetic sites of opposite spin in the unit cell are related by a rotation operation. Spin degeneracy is maintained along some symmetry lines in agreement with the group theoretical predictions described in [35]

We presented a detailed study of the exchange interactions extracted from the transverse spin susceptibility calculated in linear response from the QSGW wavefunctions and eigenvalues, which is then averaged over atomic sites and mapped onto a Heisenberg-type spin-Hamiltonian following the approach of Kotani and van Schilfhaarde [19]. This confirms the dominance of a strong antiferromagnetic coupling of order  $-1$  mRy between the two Mn in the primitive cell. The Néel temperature is calculated in both mean field and RPA approximations and estimated to be about 180 K within a classical treatment of the spin dynamics. It could be higher of order 250 K if we include a quantum correction factor. We also calculated the spin wave dispersion and the associated dynamical spin susceptibility and find, as expected, linear behavior of the spin waves near the  $\Gamma$ -point and a maximum spin wave energy of about 50 meV near the Brillouin zone boundary, of the same order of magnitude as in MnO.

We next studied several possible mechanisms which could explain the occurrence of ferromagnetism in real samples in spite of the antiferromagnetic ground state of the perfect crystal. We found that carrier mediated ferromagnetic coupling cannot explain the occurrence of ferromagnetism. While adding electrons or holes in a rigid band structure does lower the main AFM coupling, unrealistically high doping concentrations would be re-

quired to flip the sign of the coupling. On the other hand,  $\text{Mn}_{\text{Ge}}$  antisites were found to induce ferromagnetic coupling with nearby regular Mn sites. These interactions were the strongest with the nearest neighbor same spin Mn in the same basal plane and of order 1 mRy, while they are an order of magnitude smaller with the opposite spin nearest neighbors. This indicates that clusters of parallel spin are likely to occur near such antisites and could lead to dilute semiconductor type ferrimagnetism if these defects occur in a sufficient concentration to be above the percolation limit. However, these clusters of locally parallel spins would still be embedded in an overall antiferromagnetic host. On the other hand a MnP layer inserted inside AFM  $\text{MnGeP}_2$  was also found to give strong ferromagnetic coupling and with a ferrimagnetic critical temperature larger than that of actual MnP. However, even in this case we argued that the remaining antiferromagnetic couplings between regular Mn sites would maintain the antiferromagnetic ordering among alternate (001) planes. We also find that these models with  $\text{Mn}_{\text{Ge}}$  antisites have metallic band structure or show partially filled defect bands which will tend to give p-type conduction. While thus far all experimentally realized samples of  $\text{MnGeP}_2$  show ferromagnetic behavior which has usually been ascribed to a secondary MnP phase, and show metallic behavior, it would be of great interest to realize more perfect defect free  $\text{MnGeP}_2$  with a semiconducting band structure to test the predicted antiferromagnetism and in fact altermagnetism as well as the spin wave spectra we have calculated.

**Data availability Statement** The digital data related to the figures are available on <https://github.com/Electronic-Structure-Group/MnGeP2>

#### ACKNOWLEDGMENTS

This work was supported by the U.S. Department of Energy Basic Energy Sciences (DOE-BES) under Grant No. DE-SC0008933. Calculations made use of the High Performance Computing Resource in the Core Facility for Advanced Research Computing at Case Western Reserve University. J.J. acknowledges support under the CCP9 project Computational Electronic Structure of Condensed Matter [part of the Computational Science Centre for Research Communities (CoSeC)].

- 
- [1] G. A. Medvedkin, T. I. T. Ishibashi, T. N. T. Nishi, K. H. K. Hayata, Y. H. Y. Hasegawa, and K. S. K. Sato, Room Temperature Ferromagnetism in Novel Diluted Magnetic Semiconductor  $\text{Cd}_{1-x}\text{Mn}_x\text{GeP}_2$ , *Japanese Journal of Applied Physics* **39**, L949 (2000).
- [2] K. Sato, G. A. Medvedkin, T. Nishi, Y. Hasegawa, R. Misawa, K. Hirose, and T. Ishibashi, Ferromagnetic phenomenon revealed in the chalcopyrite semi-

conductor  $\text{CdGeP}_2\text{:Mn}$ , *Journal of Applied Physics* **89**, 7027 (2001), [https://pubs.aip.org/aip/jap/article-pdf/89/11/7027/19011911/7027\\_1\\_online.pdf](https://pubs.aip.org/aip/jap/article-pdf/89/11/7027/19011911/7027_1_online.pdf).

- [3] G. Medvedkin, K. Hirose, T. Ishibashi, T. Nishi, V. Voevodin, and K. Sato, New magnetic materials in  $\text{ZnGeP}_2\text{-Mn}$  chalcopyrite system, *Journal of Crystal Growth* **236**, 609 (2002).
- [4] K. Sato, G. Medvedkin, T. Ishibashi, S. Mitani,

- K. Takanashi, Y. Ishida, D. Sarma, J. Okabayashi, A. Fujimori, T. Kamatani, and H. Akai, Novel Mn-doped chalcopyrites, *Journal of Physics and Chemistry of Solids* **64**, 1461 (2003), 13th International Conference on Ternary and Multinary Compounds.
- [5] P. G. Baranov, S. I. Goloshchapov, G. A. Medvedkin, T. Ishibashi, and K. Sato, Magnetic Resonance in ZnGeP<sub>2</sub> and (Zn,Mn)GeP<sub>2</sub>, *Journal of Superconductivity* **16**, 131 (2003).
- [6] V. Popov and G. Medvedkin, Hole transport anomaly in high-TC ferromagnet (Zn,Mn)GeP<sub>2</sub>, *Solid State Communications* **132**, 561 (2004).
- [7] Y. Ishida, D. D. Sarma, K. Okazaki, J. Okabayashi, J. I. Hwang, H. Ott, A. Fujimori, G. A. Medvedkin, T. Ishibashi, and K. Sato, In situ Photoemission Study of the Room Temperature Ferromagnet ZnGeP<sub>2</sub>:Mn, *Phys. Rev. Lett.* **91**, 107202 (2003).
- [8] G. Medvedkin, Radiative transitions in undoped and Mn-doped CdGeP<sub>2</sub> crystals, *Phys. Rev. B* **109**, 205206 (2024).
- [9] G. Medvedkin, K. Sato, and T. Ishibashi, Direct evidence for a nonzero energy gap and half-metallicity in the diamondlike ferromagnet (Zn,Mn)GeP<sub>2</sub>, *Phys. Rev. B* **110**, 064406 (2024).
- [10] Y.-J. Zhao, W. T. Geng, A. J. Freeman, and T. Oguchi, Magnetism of chalcopyrite semiconductors: Cd<sub>1-x</sub>Mn<sub>x</sub>GeP<sub>2</sub>, *Phys. Rev. B* **63**, 201202 (2001).
- [11] P. Mahadevan and A. Zunger, Ferromagnetism in Mn-doped GaAs due to substitutional-interstitial complexes, *Phys. Rev. B* **68**, 075202 (2003).
- [12] K. Sato, T. Ishibashi, K. Minami, H. Yuasa, J. Jogo, T. Nagatsuka, A. Mizusawa, Y. Kangawa, and A. Koukitsu, MBE growth of a novel chalcopyrite-type ternary compound MnGeP<sub>2</sub>, *Journal of Physics and Chemistry of Solids* **66**, 2030 (2005), the 14th International Conference on Ternary and Multinary Compounds.
- [13] S. Cho, S. Choi, G.-B. Cha, S. C. Hong, Y. Kim, A. J. Freeman, J. B. Ketterson, Y. Park, and H.-M. Park, Synthesis of new pure ferromagnetic semiconductors: MnGeP<sub>2</sub> and MnGeAs<sub>2</sub>, *Solid State Communications* **129**, 609 (2004).
- [14] H. J. von Bardeleben, G. Medvedkin, P. G. Schunemann, and K. T. Zawilski, Magnetic properties of polycrystalline bulk crystals of MnGeP<sub>2</sub>, *Journal of Applied Physics* **136**, 073901 (2024).
- [15] M. van Schilfgaarde, T. Kotani, and S. Faleev, Quasiparticle Self-Consistent GW Theory, *Phys. Rev. Lett.* **96**, 226402 (2006).
- [16] T. Kotani, M. van Schilfgaarde, and S. V. Faleev, Quasiparticle self-consistent GW method: A basis for the independent-particle approximation, *Phys. Rev. B* **76**, 165106 (2007).
- [17] L. Hedin, New method for calculating the one-particle green's function with application to the electron-gas problem, *Phys. Rev.* **139**, A796 (1965).
- [18] L. Hedin and S. Lundqvist, Effects of electron-electron and electron-phonon interactions on the one-electron states of solids, in *Solid State Physics, Advanced in Research and Applications*, Vol. 23, edited by F. Seitz, D. Turnbull, and H. Ehrenreich (Academic Press, New York, 1969) pp. 1–181.
- [19] T. Kotani and M. van Schilfgaarde, Spin wave dispersion based on the quasiparticle self-consistent GW method: NiO, MnO and  $\alpha$ -MnAs, *Journal of Physics: Condensed Matter* **20**, 295214 (2008).
- [20] S. V. Tyablikov, Retarded and advanced Green functions in the theory of ferromagnetism., *Ukr. Mat. Zh.* **11**, 287 (1959).
- [21] H. B. Callen, Green Function Theory of Ferromagnetism, *Phys. Rev.* **130**, 890 (1963).
- [22] J. Ruzs, I. Turek, and M. Diviš, Random-phase approximation for critical temperatures of collinear magnets with multiple sublattices: GdX compounds ( $X = \text{Mg, Rh, Ni, Pd}$ ), *Phys. Rev. B* **71**, 174408 (2005).
- [23] D. Pashov, S. Acharya, W. R. Lambrecht, J. Jackson, K. D. Belashchenko, A. Chantis, F. Jamet, and M. van Schilfgaarde, Questaal: A package of electronic structure methods based on the linear muffin-tin orbital technique, *Computer Physics Communications*, 107065 (2019).
- [24] S. Ismail-Beigi, Justifying quasiparticle self-consistent schemes via gradient optimization in baym-kadanoff theory, *Journal of Physics: Condensed Matter* **29**, 385501 (2017).
- [25] B. Cunningham, M. Grüning, P. Azarhoosh, D. Pashov, and M. van Schilfgaarde, Effect of ladder diagrams on optical absorption spectra in a quasiparticle self-consistent GW framework, *Phys. Rev. Materials* **2**, 034603 (2018).
- [26] B. Cunningham, M. Grüning, D. Pashov, and M. van Schilfgaarde, QSGW: Quasiparticle self-consistent GW with ladder diagrams in W, *Phys. Rev. B* **108**, 165104 (2023).
- [27] F. Aryasetiawan and O. Gunnarsson, Product-basis method for calculating dielectric matrices, *Phys. Rev. B* **49**, 16214 (1994).
- [28] A. Liechtenstein, M. Katsnelson, V. Antropov, and V. Gubanov, Local spin density functional approach to the theory of exchange interactions in ferromagnetic metals and alloys, *Journal of Magnetism and Magnetic Materials* **67**, 65 (1987).
- [29] F. Aryasetiawan and K. Karlsson, Green's function formalism for calculating spin-wave spectra, *Phys. Rev. B* **60**, 7419 (1999).
- [30] E. Şaşıoğlu, L. M. Sandratskii, and P. Bruno, First-principles calculation of the intersublattice exchange interactions and Curie temperatures of the full Heusler alloys Ni<sub>2</sub>MnX ( $X = \text{Ga, In, Sn, Sb}$ ), *Phys. Rev. B* **70**, 024427 (2004).
- [31] G. Onida, L. Reining, and A. Rubio, Electronic excitations: density-functional versus many-body Green's-function approaches, *Rev. Mod. Phys.* **74**, 601 (2002).
- [32] W. Hanke, Dielectric theory of elementary excitations in crystals, *Advances in Physics* **27**, 287 (1978).
- [33] G. Strinati, Application of the Green's functions method to the study of the optical properties of semiconductors, *La Rivista del Nuovo Cimento* (1978-1999) **11**, 1 (1988).
- [34] M. Rohlfing and S. G. Louie, Electron-hole excitations and optical spectra from first principles, *Phys. Rev. B* **62**, 4927 (2000).
- [35] L. Šmejkal, J. Sinova, and T. Jungwirth, Emerging Research Landscape of Altermagnetism, *Phys. Rev. X* **12**, 040501 (2022).
- [36] L.-D. Yuan, Z. Wang, J.-W. Luo, E. I. Rashba, and A. Zunger, Giant momentum-dependent spin splitting in centrosymmetric low-Z antiferromagnets, *Phys. Rev. B* **102**, 014422 (2020).